

See discussions, stats, and author profiles for this publication at: <https://www.researchgate.net/publication/236221419>

Fluid Structure Interaction Simulation of Spinnakers – Getting Closer to Reality

Article in *The International Journal of Small Craft Technology* · July 2011

DOI: 10.3940/rina.ijst.2011.b2.115

CITATIONS

17

READS

496

2 authors:



Hannes Renzsch

FluidEngineeringSolutions GmbH & Co. KG

17 PUBLICATIONS 114 CITATIONS

[SEE PROFILE](#)



Kai Graf

Fachhochschule Kiel

32 PUBLICATIONS 220 CITATIONS

[SEE PROFILE](#)

Some of the authors of this publication are also working on these related projects:



Continuing development of OpenFoam Solver for Ship Hydrodynamics [View project](#)



FlexSail [View project](#)

FLUID STRUCTURE INTERACTION SIMULATION OF SPINNAKERS – GETTING CLOSER TO REALITY

(DOI No: 10.3940/rina.ijsc.2011.b2.115)

H F Renzsch, Technical University Delft, The Netherlands
K U Graf, University of Applied Sciences Kiel, Germany

SUMMARY

This paper describes the current implementation of FlexSail, a Fluid-Structure-Interaction program for the simulation of the behaviour of spinnakers. A short outline of general membrane theory is given, the major focus lies on the impact of wrinkling and validation. A numerical modelling of anisotropic wrinkling is presented, its impact on flying shape and flow forces investigated. A newly implemented solver is described. A series of test cases comparing the numerical results to data from the Yacht Research Unit Kiel Twisted Flow Wind Tunnel is presented and discussed.

NOMENCLATURE

a	scalar
\mathbf{a}	vector
\mathbf{A}	matrix
\wedge	material coordinate system
$-$	element coordinate system
\sim	wrinkled coordinate system
xx, yy, xy	element axes
$11, 22, 12$	material axes
φ	in orientation of φ
AWA	apparent wind angle [deg]
AWS	apparent wind speed [m s^{-1}]
ε	strain
$\varepsilon_1, \varepsilon_2, \sigma_1, \sigma_2$	principal strains, stresses [N m^{-1}]
E	Young's modulus [N m^{-1}]
G	shear modulus [N m^{-1}]
\mathbf{H}	Hessian matrix
φ	rotation angle
m_i	virtual mass of node i
ν	Poisson number
P_{Dyn}	dynamic pressure [N m^{-2}]
\mathbf{R}_i	total force on node i (residual)
ρ_{Air}	density of air [kg m^{-3}]
σ	stress [N m^{-1}]
σ_m	material stress [N m^{-1}]
t	at time t
\mathbf{V}_i	velocity of node i
\mathbf{x}_i	displacement of node i
y^+	dimensionless wall distance

1. INTRODUCTION

Typically, new spinnaker designs are evaluated by wind tunnel testing. Due to the problems associated with the simulation of the partially separated flow usually found around spinnakers, numerical investigation of a new design is currently still a niche application.

Simulations of the flow around sails, in particular spinnakers not only have to cope with the problem of flow separation, they also have to account for the large

displacements of the sail under wind load. Thus fluid structure interaction is needed.

The historical development of Fluid-Structure-Interaction codes for the simulations of upwind sails lead to a split between structural and flow code that made sense for applications where the structural code needed the majority of the computational power. Usually the two codes were either coupled in batch mode or the structural code triggers the flow code, both codes in turn calculating until convergence individually.

These structural codes have been successfully coupled with RANSE codes in the past, yet, due to both codes calculating until convergence on each iteration, computation costs for the simulation were extremely high and practical solutions were limited to steady state.

FlexSail is a Fluid-Structure-Interaction program specifically designed to include a RANSE solver as flow code and still run in an efficient manner. To this end a different coupling paradigm, suited to the high computational costs of RANSE simulations, is used. This method is able to simulate a quasi-steady state as well as globally instationary behaviour of spinnakers, capable to solve global instationarity or stability problems associated with downwind sail operation.

2. FLEXSAIL – BASIC IDEA

Like any other Fluid-Structure-Interaction program FlexSail iterates the flow and structural solver to find equilibrium in both solutions and a converged state in the coupling of both. Flow is computed using the commercial flow solver AnsysCFX 12.0, a program for the simulation of viscous flow by solving the steady or unsteady RANSE equations. The structural behaviour is simulated by a purpose-written membrane finite element code, capable of simulating large displacements and highly non-linear behaviour. It is embedded in the RANSE solver.

What sets FlexSail apart from other FSI solution methods is the coupling paradigm. The basic idea is to run the flow simulation in an unsteady mode. That means that

each timestep is considered a valid solution. Therefore the structural code can be called from within the flow code repeatedly at given timesteps of the flow solution. See Figure 1 for a flow chart of the process.

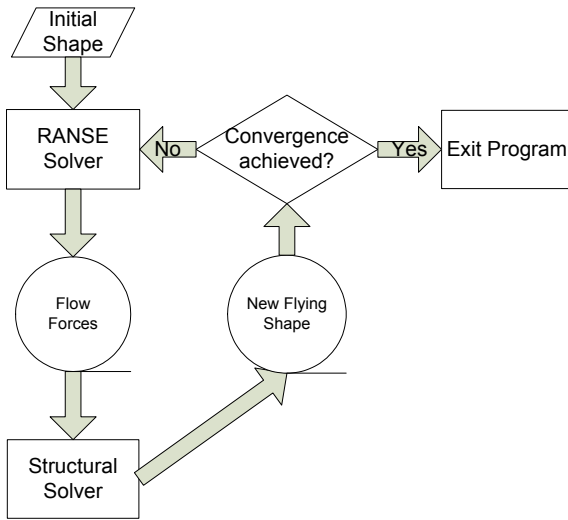


Figure 1: Flow Chart of FSI process

The coupling utilises two interfaces provided by CFX: *User CEL Routine* and *Junction Box Routine*. The two interfaces differ in their capabilities and the way they are called [13]:

- The *User CEL Routine* provides a direct interface to data used by CFX. It is called from within CFX at a point during the calculation determined by CFX from the data used and allows out- and input of selected data as calling arguments. It is called by each partition individually for the data used by that partition.
- The *Junction Box Routine* is called from CFX at a point determined by the user. It does not provide any calling arguments. What is provided is full access to the *CFX Memory Management System* (MMS), the system used to manage all calculation data. While being called individually by each partition as well, it allows to transfer data between partition using the *Parallel Virtual Machine* (PVM) setup used by CFX for its own communication.

A *User CEL Routine* called from the mesh deformation loop is used to write and read the nodal pressures and locations to and from a user defined section of the local MMS of each partition. A *Junction Box Routine* is used to transfer all nodal pressure data to the master partition, initiate the FE-run (local) and return the new nodal coordinates to each partition via PVM. Most probably this is not the most elegant way but it is robust.

The coupling method (fully explicit) results in a weak two-way coupling between flow and structural simulation. Therefore the timestep length has to be significantly smaller than any natural periods of dynamic

occurrences considered in dynamic simulations. A typical application is shown in [1].

3. DESCRIPTION OF THE CST ELEMENT

3.1 GENERAL

Generally the stress – strain relationship is given by:

$$\boldsymbol{\sigma} = \mathbf{H} \cdot \boldsymbol{\varepsilon}$$

with $\boldsymbol{\varepsilon} = \{\varepsilon_{xx}; \varepsilon_{yy}; \sqrt{2}\varepsilon_{xy}\}^T$ and $\boldsymbol{\sigma} = \{\sigma_{xx}; \sigma_{yy}; \sqrt{2}\sigma_{xy}\}^T$.

The factor $\sqrt{2}$ is included just for mathematical convenience later on.

To discretise the sail, Constant Stress Triangle elements as described in Figure 2 are used.

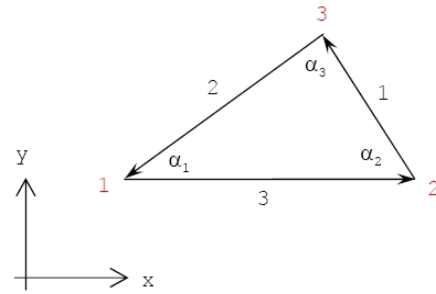


Figure 2: Description of triangle element

Note that edge 3 is parallel to the x-axis.

In FlexSail linear Hookean materials are assumed. The generalised stress-strain relationship, the Hessian matrix $\hat{\mathbf{H}}$, for the linear behaviour of an arbitrary material in material coordinate system 1-2 (see Figure 3) is the partial derivative of stress by strain and can be written as:

$$\hat{\mathbf{H}} = \begin{bmatrix} \frac{\partial \sigma_{11}}{\partial \varepsilon_{11}} & \frac{\partial \sigma_{11}}{\partial \varepsilon_{22}} & \frac{\partial \sigma_{11}}{\partial \varepsilon_{12}} \\ \frac{\partial \sigma_{22}}{\partial \varepsilon_{11}} & \frac{\partial \sigma_{22}}{\partial \varepsilon_{22}} & \frac{\partial \sigma_{22}}{\partial \varepsilon_{12}} \\ \frac{\partial \sigma_{12}}{\partial \varepsilon_{11}} & \frac{\partial \sigma_{12}}{\partial \varepsilon_{22}} & \frac{\partial \sigma_{12}}{\partial \varepsilon_{12}} \end{bmatrix}$$

This linear description of element stress-strain relationship only holds true under the assumption of small strains.

The stress strain relations for arbitrary directions, where the material directions have been rotated a positive angle φ from the x-axis (see Figure 3), can be written as follows:

$$\bar{\boldsymbol{\sigma}} = \mathbf{T}^{-1} \cdot \hat{\mathbf{H}} \cdot \mathbf{T} \cdot \bar{\boldsymbol{\varepsilon}}$$

With \mathbf{T} being the transformation matrix from element to material coordinate system:

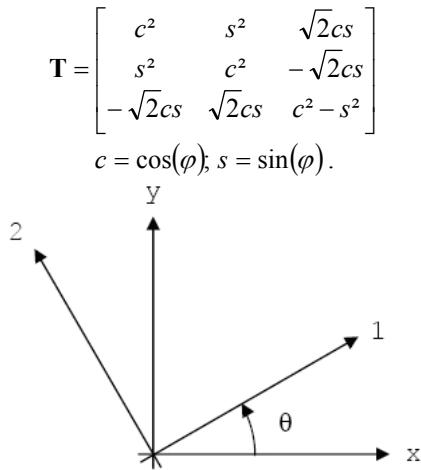


Figure 3: Element and material coordinate systems

A more detailed description of the structural method is given in [2] and [3].

4. ANISOTROPIC WRINKLING

A significant shortcoming of the basic membrane stress – strain formulation is its behaviour under compressive in-plane loads. “Real” sailcloth has a negligible bending stiffness and therefore negligible buckling strength, with compressive in-plane loads causing the cloth to wrinkle. Unfortunately, the basic membrane formulation has the same stress-strain gradient under compression as well as under tension.

This shortcoming is corrected by using a wrinkling model. Some wrinkling models ([4], [5]) calculate the wrinkling angle directly from strains and alter the stiffness matrix in case of wrinkling. Yet, until now this approach has only been described for isotropic materials and, in fact, doesn’t replicate the real behaviour of materials. Other wrinkling models ([6], [7], [9]) modify the deformation vector under following observations:

- A wrinkled membrane is in a state of uniaxial tension.
- The wrinkles are aligned with this uniaxial tension.
- Material stresses are invariant to strain changes perpendicular to the wrinkles as long as the membrane is not coming under tension in this direction.
- In anisotropic materials principal stresses and strains are not aligned.
- If we assume the taut state as a starting point and reduce principle stress in direction two (σ_2), the basic membrane formulation holds up to - and including - the point where σ_2 is exactly zero but the material not yet wrinkled. From this point on material stress remains unchanged while element strain changes further (this assuming principle stress σ_1 being greater or equal than principle stress σ_2)

These observations lead to the mixed stress – strain wrinkling criterion

$$\sigma_2 > 0 \Rightarrow \text{taut}$$

$$\varepsilon_1 \leq 0 \Rightarrow \text{slack}$$

$$\varepsilon_1 > 0 \text{ and } \sigma_2 \leq 0 \Rightarrow \text{wrinkled}$$

and following modification of the membrane formulation assuming uniaxial tension in direction φ .

$$\boldsymbol{\sigma}_m^\varphi = \mathbf{H}^\varphi \cdot (\boldsymbol{\varepsilon}^\varphi + \boldsymbol{\varepsilon}_w^\varphi)$$

$$\text{with the material stress } \boldsymbol{\sigma}_m^\varphi = \begin{Bmatrix} \sigma_{m11}^\varphi \\ 0 \\ 0 \end{Bmatrix}$$

$$\text{and the wrinkling strain } \boldsymbol{\varepsilon}_w^\varphi = \begin{Bmatrix} 0 \\ \varepsilon_{w22}^\varphi \\ 0 \end{Bmatrix}, \text{ where } \varepsilon_{w22}^\varphi \text{ is a}$$

measure for the amount of wrinkling.

Geometrically this modification can be described as shown in Figure 4:

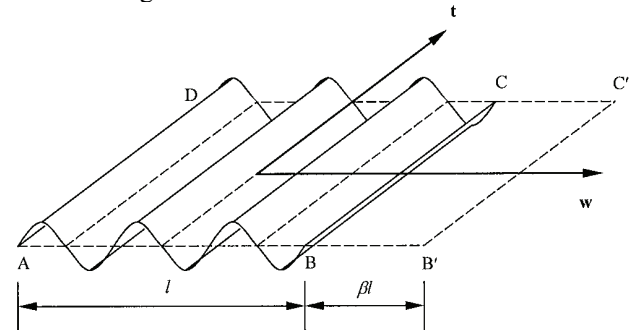


Figure 4: material under *natural* uniaxial tension (AB'C'D) and uniaxial tension (wrinkled, ABCD) [5]

ABCD are the corners of a wrinkled membrane element under uniaxial tension in direction \mathbf{t} . Material stress in direction \mathbf{w} is zero, yet strain in direction \mathbf{w} is negative finite. If we extend the membrane direction \mathbf{w} exactly up to the point where the wrinkles vanish but material stress is still zero (AB'C'D), we find the state of *natural* uniaxial tension. Up to this state material stress is invariant, yet from this state on the regular membrane formulation holds true.

In the state of *natural* uniaxial tension we can write:

$$\boldsymbol{\sigma}_m^\varphi = \mathbf{H}^\varphi \cdot \boldsymbol{\varepsilon}^\varphi$$

Defining $\boldsymbol{\sigma}_m^\varphi = \{\sigma_{m11}^\varphi; 0; 0\}^T$ we can rewrite:

$$\varepsilon_{22}^\varphi = \frac{H_{21}^\varphi H_{33}^\varphi - H_{23}^\varphi H_{31}^\varphi}{H_{23}^\varphi H_{32}^\varphi - H_{22}^\varphi H_{33}^\varphi} \cdot \varepsilon_{11}^\varphi$$

and

$$\sqrt{2}\varepsilon_{12}^{\phi} = \frac{H_{22}^{\phi}H_{31}^{\phi} - H_{21}^{\phi}H_{32}^{\phi}}{H_{23}^{\phi}H_{32}^{\phi} - H_{22}^{\phi}H_{33}^{\phi}} \cdot \varepsilon_{11}^{\phi}$$

Under the observations above we now can state that the formulation for ε_{12}^{ϕ} holds true for general uniaxial tension, while ε_{22}^{ϕ} is restricted to *natural* uniaxial tension. As well we can state that ε_{11}^{ϕ} is the same regardless of *natural* or *general* uniaxial tension. Therefore we can calculate $\mathbf{\varepsilon}^{\phi}$ from element rotation $\tilde{\mathbf{\varepsilon}}^{\phi} = \mathbf{T} \cdot \mathbf{\varepsilon}$ or $\tilde{\mathbf{\varepsilon}}^{\phi}$ for the state of *natural* uniaxial tension from the above formulae with $\tilde{\varepsilon}_{11}^{\phi} = \tilde{\varepsilon}_{11}^{\phi}$.

Given the two methods to determine $\mathbf{\varepsilon}$, now we have to numerically find the angle ϕ where, under the condition of $\tilde{\varepsilon}_{11}^{\phi} = \tilde{\varepsilon}_{11}^{\phi}$, ε_{11} is positive definite, $\tilde{\varepsilon}_{12}^{\phi} = \tilde{\varepsilon}_{12}^{\phi}$ and $\tilde{\varepsilon}_{22}^{\phi} \geq \tilde{\varepsilon}_{22}^{\phi}$. ε_{w22}^{ϕ} is given by $\varepsilon_{w22}^{\phi} = \tilde{\varepsilon}_{22}^{\phi} - \tilde{\varepsilon}_{22}^{\phi}$ and is always positive finite. At this angle the above condition for σ_m^{ϕ} will be fulfilled. This is done by bracketing of the roots [14] as recommended in [6] and using Ridders's method to find it to a predefined degree (e.g. 0.01*pi). Assuming the case of a wrinkled element two roots are returned, one gives the angle of σ_1 from the material axes the other the angle of σ_2 . ϕ is determined by checking the values of ε_{11}^{ϕ} and ε_{22}^{ϕ} at these angles. This approach is quite stable as long as the structural properties of axes of the sail's material are basically balanced (meaning not uni-directional).

For the special case of an isotropic material ϕ can be calculated directly from the directional strains $\mathbf{\varepsilon}$ by

$$\tan(2\phi) = \frac{2\varepsilon_{12}}{\varepsilon_{11} - \varepsilon_{22}}$$

In the current (debug) implementation, the analysis of anisotropic wrinkling increases runtime four to five times compared to a purely isotropic wrinkling analysis. This is due to the computational effort for finding the wrinkling angle numerically as opposed to direct calculation and depends a lot on the fraction of wrinkled elements in the total structure.

5. FE – SOLVER

The solver used so far for the structural part of FlexSail was based on the minimization of total potential energy using a modified Newton approach [2]. However it was not able to treat the strong structural nonlinearities associated with wrinkling. Thus a new solver has been implemented.

Promising the necessary stability, a kinetically damped *Dynamic Relaxation* approach was chosen to solve the finite-element case [8]. In this approach separate equations for equilibrium and compatibility are used. The

structure is described by a dampened vibrating system with virtual masses on the nodes and link forces to describe the elements. The solution then is based on a time strepping scheme.

Basically the motion of any node i at time t can be described by Newton's 2nd law of motion as

$$\dot{\mathbf{V}}_i^t = \frac{\mathbf{R}_i^t}{m_i}$$

with \mathbf{R}_i^t being the vectorial sum of all forces (internal and external) acting on node i at time t .

In centred difference form this acceleration term can be approximated as:

$$\dot{\mathbf{V}}_i^t = \frac{\mathbf{V}_i^{t+\Delta t/2} - \mathbf{V}_i^{t-\Delta t/2}}{\Delta t}$$

This yields the following term for nodal velocities at time $(t + \Delta t/2)$:

$$\mathbf{V}_i^{t+\Delta t/2} = \mathbf{V}_i^{t-\Delta t/2} + \Delta t \cdot \frac{\mathbf{R}_i^t}{m_i}$$

The updated geometry projected to time $(t + \Delta t)$ is therefore given by:

$$\mathbf{x}_i^{t+\Delta t} = \mathbf{x}_i^t + \Delta t \cdot \mathbf{V}_i^{t+\Delta t/2}$$

The isotropic virtual masses used above are calculated by

$$m_i = \frac{\Delta t^2}{2} \cdot S_i$$

With S_i being the largest direct stiffness that may occur during analysis.

To get the dynamic relaxation solver to converge some kind of damping method is necessary. Typically used is either viscous or kinetic damping. For FlexSail kinetic damping was chosen as it gives robust performance with little computational overhead. In a kinetically damped system kinetic energy peaks of the whole vibrating system are detected and all nodal velocities set to zero before releasing the nodes again.

As described in [8], due to “the separation of equilibrium and compatibility” giving a vectorial formulation of the problem, no global stiffness matrix has to be constructed, keeping computational overhead low. The vectorial formulation lends itself to parallelising using a SPMD paradigm on a multi-core machine. An initial, unoptimised OpenMP implementation has shown a significant reduction of runtime.

6. IMPACT OF WRINKLING

Wrinkling has a dramatic impact on the shape of the sail. As shown in [9], in the case of upwind sails the occurrence of wrinkling, voluntary or involuntary, can have a significant effect on the amount of draft, its position and entry and exit angles. In [9] this is attributed to the physical model as well as grid kinematics effects.

In the case of a spinnaker, where the sail's displacements and changes in surface curvature are significantly larger, the effect of including a wrinkling model can be observed in a dramatic fashion.

To show the effects flying shapes under constant pressure difference were calculated for a symmetric spinnaker with significant tack displacement and sheet length change. In Figure 5 the designed shape of the investigated spinnaker is shown. For discretization a triangular net of 7250 elements is used.

Figure 6 gives the flying shapes without and with wrinkling model.

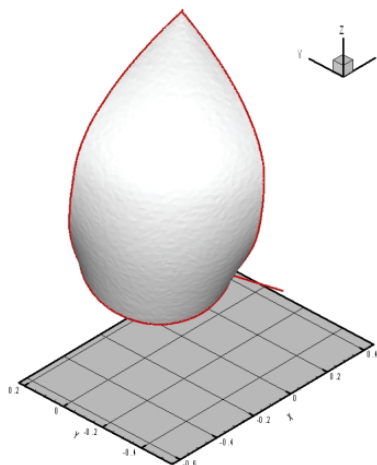


Figure 5: Mould of tested spinnaker (design shape)

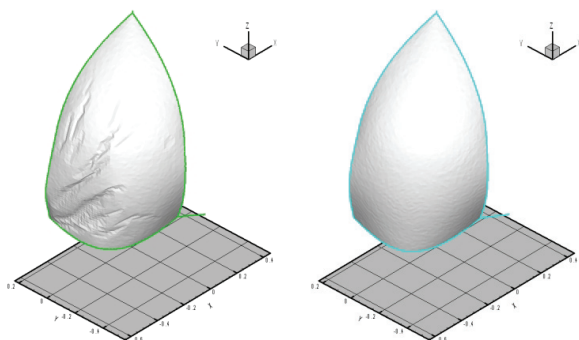


Figure 6: Flying shapes without (left) and with (right) wrinkling model

It can be seen that without accounting for wrinkling (Figure 6, left), significant folds radiate from the tack. Under strong Gaussian deformations the membrane without wrinkling model appears to behave like a thin

sheet of plastic or metal under compression. Figure 6, right does not show this behaviour. Wrinkling is not visible as it occurs on a sub-element scale.

Figures 7 and 8 show principal stresses in direction 1 and 2. With wrinkling model the principal stresses 1 mostly radiate out from the corners and go up the side leeches, dissipating towards the centre of the sail. Principal stresses 2 are oriented perpendicular to them and equal or larger than zero. Without wrinkling model the principal stresses 1 are primarily oriented along the folds with significantly negative principal stresses 2 across the folds.

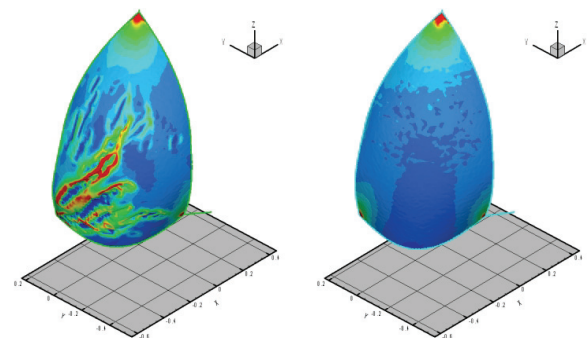


Figure 7: Principal stress 1 without and with wrinkling model

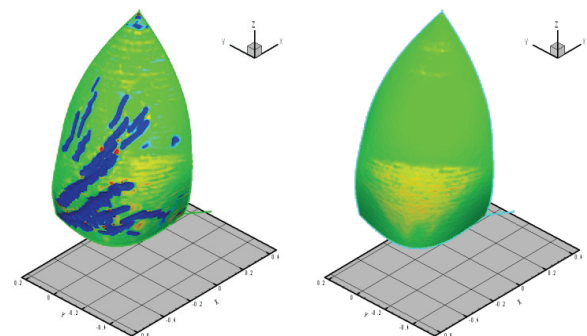


Figure 8: Principal stress 2 without and with wrinkling model

The folds can be attributed to an effect known as *grid-locking*. This effect typically occurs on low-order triangular membrane or shell elements without a wrinkling model. These elements have the particular property that compressive deformation is accompanied by opposing nodal forces. Higher order elements can deform conically (e.g. buckling), the wrinkling model contains the condition that compression is free of force.

This grid-locking effect imposes a restriction on nodal motion in the affected areas and therefore erroneous nodal forces and deformed shape. It is important to note that the folds cannot be seen as a representation of folds occurring on the real sail in any way as the particular size and geometry of these folds is dictated purely by the mesh resolution. To evaluate the real shape of folds occurring on the sail would necessitate modelling the sail using higher order shell elements combined with a buckling analysis.

7. CFD GRID SENSITIVITY

A grid sensitivity study for the CFD part of the simulation was carried out on a single fixed spinnaker geometry. For this study general grid resolution, boundary layer resolution and timestep length, respectively Courant number were varied. The grids consisted of tetrahedrons for the majority of the volume and prism elements for boundary layer resolution. The SST turbulence model with a turbulence level of 5% was used for all computations.

Very little dependency of forces on timestep length was observed as soon as the timestep was small enough not to induce artificial instationarities.

General grid resolution and boundary layer resolution have a much more significant impact on resultant forces. Figure 9 shows driving and side forces for the selected testcase depending on total grid size and y^+ value in the state of timestep insensitivity.

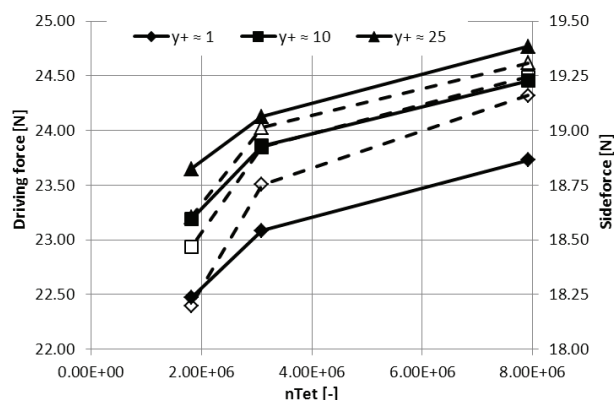


Figure 9: Driving (continuous) and side (dashed) forces depending on general grid and boundary layer resolution

While grid insensitivity has obviously not been reached, a definitive trend can be observed. Typically further refinement of the grid would be deemed necessary. Unfortunately finer grids were found to be impractical for the FSI case.

Results of grid sensitivity analyses for the FE and FSI cases are not available for publication to date.

8. VALIDATION TESTCASES

For the validation of *FlexSail* a symmetrical spinnaker was tested in the Yacht Research Unit Kiel's Twisted Flow Wind Tunnel (TFWT) [3]. This spinnaker's design was the result of a development for sailmakers *Holm Segel Schleswig/Germany*. The spinnaker design was developed as a generic mould based on a 40' cruiser/racer. During the tests it emerged to be beneficial to trade area for a more stable and controllable shape, maintaining more attached flow over a wider range of *AWAs*. Therefore the spinnaker has less than maximum surface area within the given design envelope. During

wind tunnel tests the final design has proven to be quite stable and forgiving while having driving forces comparable to maximum sized spinnakers at significantly reduces sideforces. This was corroborated during testing this spinnaker at full scale.

The tested spinnaker had the following dimensions:

SL [m] =	1.43
SMG [m] =	0.766
SF [m] =	0.808
Area [m ²] =	0.923

8.1 WIND TUNNEL TESTING AND FLYING SHAPE CAPTURING

For validation purposes, the spinnaker was tested over an *AWA*-range of 90° to 180° at an *AWS* of 5 m s⁻¹. Trim settings were recorded during the tests for use in simulations. The resulting force areas are given in Figure 10, reproducibility of the results were confirmed during tests measurements using the recorded trim settings. For scaling and comparison purposes the forces are normalized by the dynamic pressure of the apparent wind ($P_{Dyn} = 1/2 \cdot \rho_{Air} \cdot AWS^2$), resulting in force areas. The trends of the measured forces appear to be quite peculiar with significant jumps between *AWA* = 120° and 127.5°. This appears to be caused by the flow being at least partially attached to the spinnaker at *AWA* ≤ 120° and fully separated at *AWA* ≥ 127.5°. At *AWA* = 120° the spinnaker trim for maximum driving force was quite unusual, especially compared to *AWA* = 112.5° & 127.5°. At this *AWA* trimming for maximum driving force lead to an exceptionally high spinnaker pole position for keeping the upper part of the sail flat. The gap in the curves is to account for this transitional behaviour. During the tests the spinnaker sheet lead was adjusted to prevent the sheet from being deflected by the main boom.

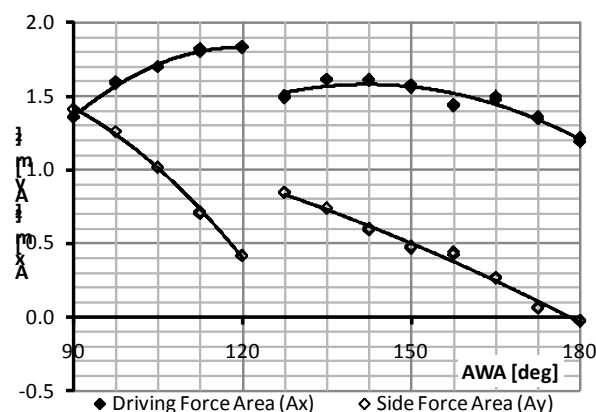


Figure 10: Driving and side force areas for spinnaker and main sail from TFWT-measurements

The general arrangement of the TFWT is shown in Figure 11.

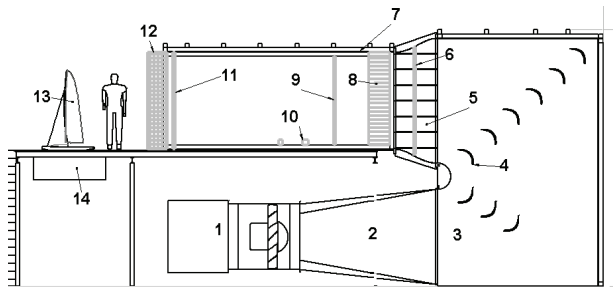


Figure 11: General arrangement of YRU-Kiel Twisted Flow Wind Tunnel

During the TFWT measurements the flying shape of main sail and spinnaker was recorded using photogrammetric techniques [10]. Figure 12 shows the relation between an exemplary picture used for the measurements and the resulting CAD model. The images were processed using Photomodeller®.

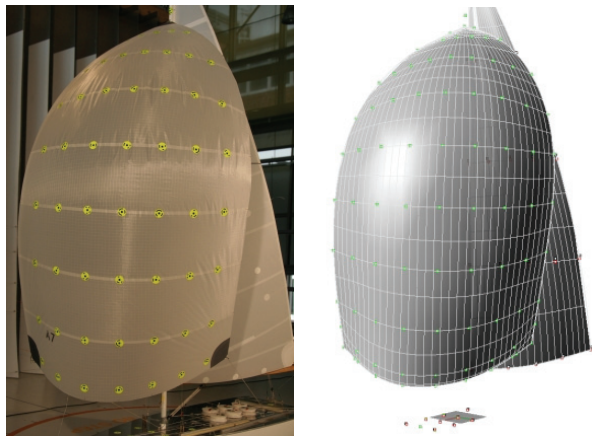


Figure 12: Exemplary photo from photogrammetric measurements and corresponding CAD model

8.2 SIMULATION USING FLEXSAIL

The flow around the main and spinnaker and the spinnakers structural behaviour were simulated using FlexSail. The simulations were carried out in model scale. For the simulations the main sail was assumed to be rigid with a flying shape as recorded during the wind tunnel tests, the spinnaker was trimmed according to the settings recorded during these measurements. To ensure comparability the incident flow was modelled based on measurements of the wind tunnel flow conditions. The simulations were carried out at model scale to keep Reynold's-similarity. The structural properties of the spinnaker were the same as in the wind tunnel.

The discretisation mesh for the spinnaker consisted of 12479 triangular elements with local refinement near the three corners of the sail. Total control volumes in the domain numbered approx. $2.2 \cdot 10^6$, this includes refinement by prism cells close to sails and hull to resolve the boundary layer. On the spinnaker the same surface mesh is used for the structural computations and the flow simulation. In all flow simulations the typical y^+ was between 1 and 4, the average Courant Number was

around 30. Following the findings from simulations of the Wilkinson testcase, the SST turbulence model was used with a free stream turbulence of 5%.

Figure 13 shows the design output from the sailmaker's lofting program ProSail.

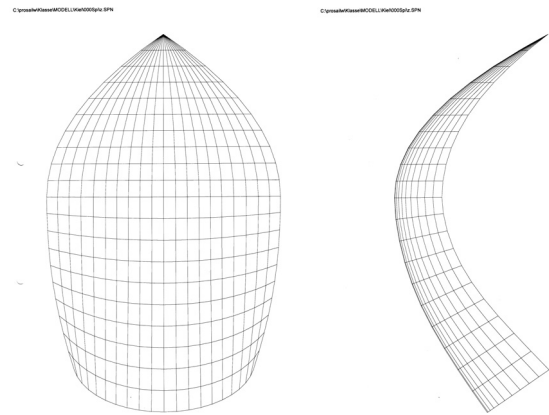


Figure 13: Designed shape from ProSail

The result of the simulation shows a significant change from designed shape to flying shape, Figure 14 compares design and flying shape at AWA = 90°.

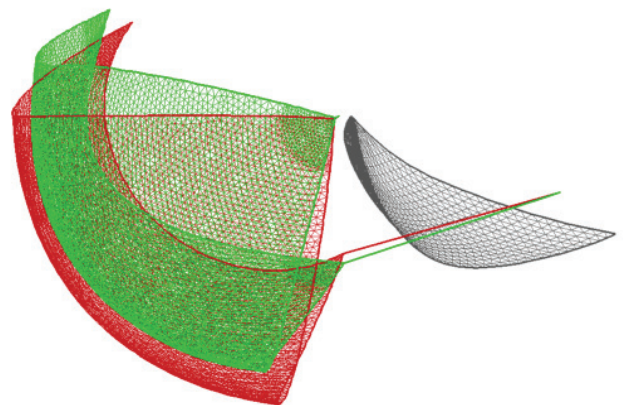


Figure 14: Designed (red) and computed flying (green) shape at AWA = 90°

This comparison indicates a significant displacement respectively change of shape from designed to flying shape. Especially the projection of the luff can be clearly seen.

The streamlines in Figure 15 show clean flow behaviour around the body of the spinnaker. Only near head, foot and close to the leech some divergence of the streamlines is visible, indicating separation in these areas. This is supported by the pressure distribution shown in Figure 16. Near the luff an area of low pressure can be observed indicating a suction peak. The interruption of this area close to mid-luff indicates a locally non-optimum luff twist distribution. The pressure increases gradually towards the leech.

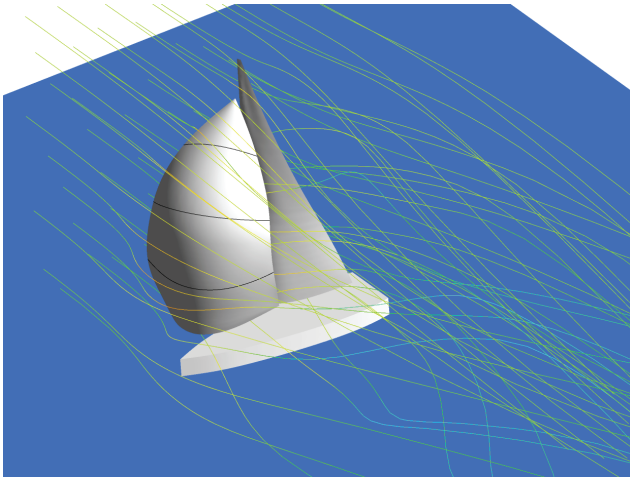


Figure 15: Streamlines around boat and sails

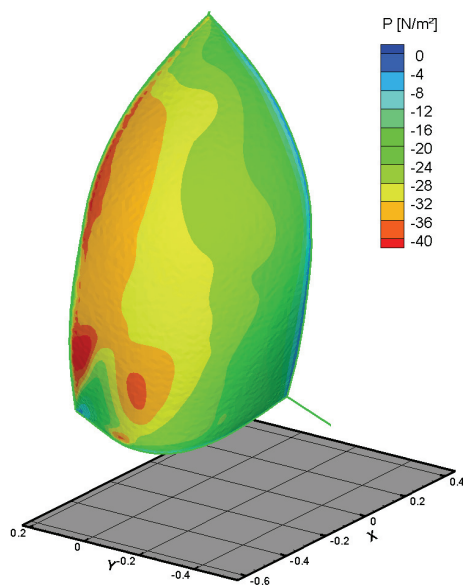


Figure 16: Pressure distribution on spinnaker

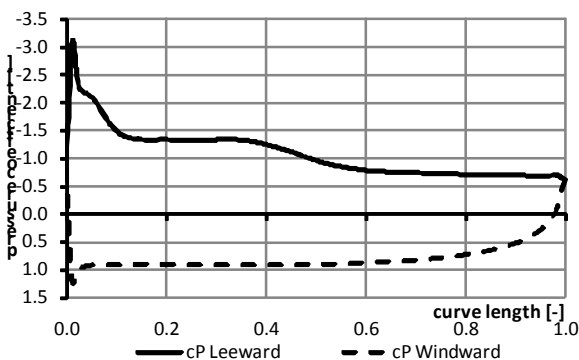


Figure 17: Typical pressure distribution on both sides of spinnaker with partially detached flow

Figure 17 gives a typical pressure distribution along a girth line for both sides of the sail. While the pressure distribution on the suction (leeward) side is highly dependent on the actual flow conditions, it is always virtually the same on the pressure (windward) side. Figure 18 exemplarily gives the suction side pressure distributions on a girth at half height at different AWAs.

The pressure profiles indicate either leading edge separation with following reattachment and trailing edge stall (AWA 90° & 120°) or fully separated flow (AWA 150°). Comparison with measured pressure distributions on an asymmetric spinnaker, given by Viola [11], shows good qualitative agreement.

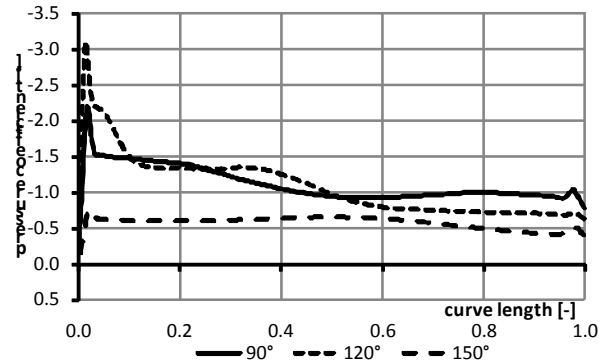


Figure 18: Pressure distributions along sail girth on 1/2 metre height at different AWAs

Figure 19 shows the distributions of principal stresses (σ_1 and σ_2) within the spinnaker. It is clearly observable that the largest stresses (areas of large σ_1) run up the luff. σ_2 is zero in large parts of the sail, yet, as the sail's size is not visibly reduced, the cloth in these areas appears to be right at the verge of wrinkling. Near the head σ_2 is larger than zero, indicating that the behaviour of the sail near the head will be quite stable. This is supported by observations during trimming in the TFWT.

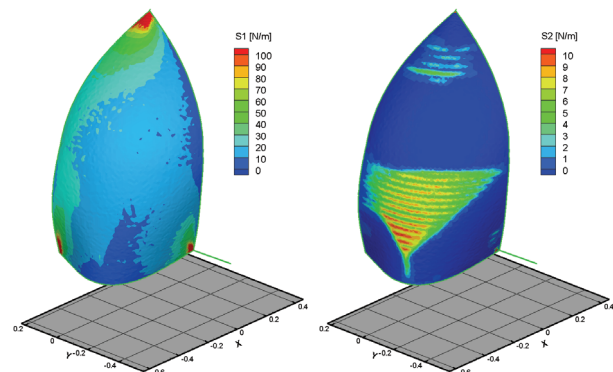


Figure 19: Principal stresses in directions one and two

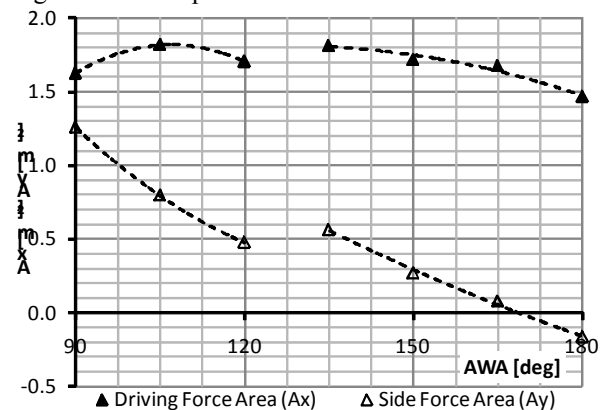


Figure 20: Force areas of sail set

Figure 20 gives the driving and side forces resulting from the simulation, calculated the same way as above. The same peculiar jumps in driving and side force area as in the wind tunnel measurements can be observed.

8.3 COMPARISON OF RESULTS

To validate the FSI simulation, flying shapes as well as forces have to be compared. Figure 21 gives a superposition of the measured and calculated flying shapes at AWAs 90° and 150°. As can be seen, the flying shapes agree well with respect to luff and leech positions and profile shapes. Table 1 gives the maximum deviations of luff, leech and clew positions as percentage of leech length. Obviously the largest deviations appear at the leech as this has the most freedom to move. The largest deviations per trim occur at AWAs 120° and 180°. As stated above, the trim at AWA 120° was quite peculiar, while at 180° the sail was a little unstable in the wind tunnel as well as during simulations.

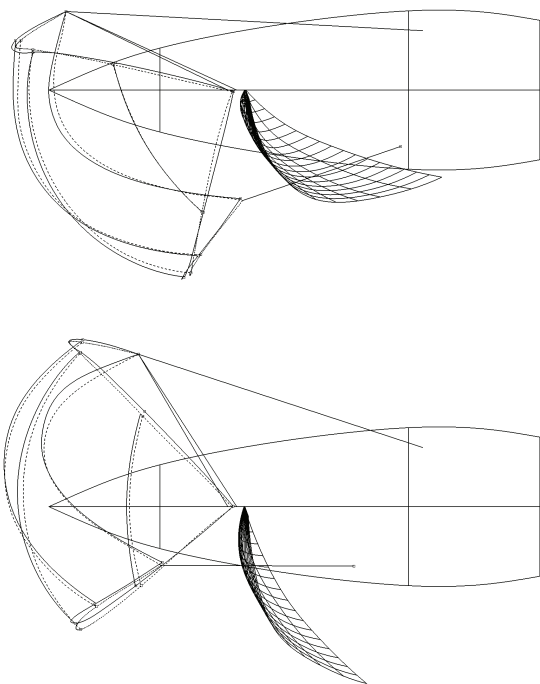


Figure 21: Comparison of flying shapes from wind tunnel (dashed) and FSI simulation (continuous) at AWA 90° (top) and 150° (bottom)

Figure 22 gives the resulting force areas from wind tunnel tests and FlexSail simulations in comparison. As can be seen the simulations mostly replicate the trends found by the wind tunnel measurements, yet at an offset. At AWA = 120° the simulation results indicate an earlier change from partially attached to fully separated flow. It is as yet unclear whether the differences are due shortcomings in the wind tunnel measurements or flow simulations. A possible reason might be the omission of

the mast in the simulations to improve meshing facility. According to Paton et al. [12], this can lead to a significant increase of lift and reduction of drag of the attached sail.

AWA	Luff	Leech	Clew
90°	0.90%	1.63%	0.49%
105°	1.39%	2.13%	0.58%
120°	1.57%	2.41%	2.40%
135°	2.17%	1.66%	1.58%
150°	1.15%	1.86%	0.83%
165°	1.11%	2.34%	1.53%
180°	1.95%	4.52%	2.20%
Avg.	1.46%	2.36%	1.37%

Table 1: Maximum deviation between measured and calculated leech and clew positions in percent of leech length

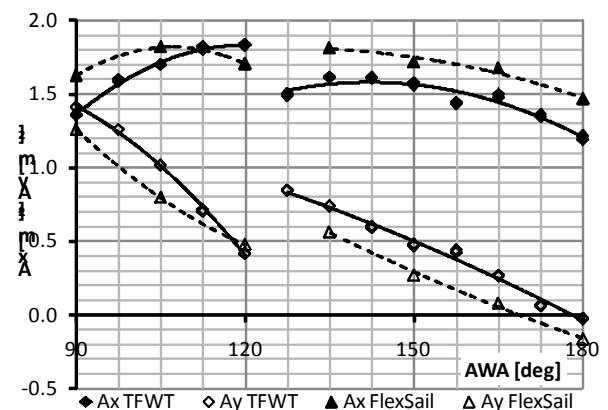


Figure 22: Driving and side forces from wind tunnel measurements and FlexSail simulations

9. CONCLUSIONS

The development of a program for the simulation of the flow around and the structural behaviour of downwind sails has been described. A physically correct wrinkling model has been detailed, a short overview of a solver, stable even at large geometrical as well as structural non-linearities, has been given.

The necessity for a wrinkling model has been shown, detailing the significance of the errors introduced by the locking effect of the basic CST-elements under compressive deformation.

The capabilities of the entire FSI method have been validated by comparison to a bespoke test case, based on measurements at the YRU-Kiel twisted flow wind tunnel. Whilst the absolute forces are a bit off, the trends are accurately replicated. The flying shape is calculated quite accurately over the whole tested range of AWAs.

Generally it can be said that the method presented is able to provide the sail designer with the information necessary to optimise the sail's design and construction.

10. REFERENCES

1. GRAF, K., BÖHM, C., RENZSCH, H., 'CFD- and VPP-Challenges in the Design of the New AC90 Americas Cup Yacht', *Proceedings 19th Chesapeake Sailing Yacht Symposium*, 2009
2. GRAF, K., RENZSCH, H., 'RANSE Investigations of Downwind Sails and Integration into Sailing Yacht Design Processes', *Proceedings 2nd High Performance Yacht Design Conference*, 2006
3. RENZSCH, H., MÜLLER, O., GRAF, K., 'FlexSail – A Fluid Structure Interaction Program for the Investigation of Spinnakers', *Proceedings Innov'Sail*, 2008
4. MILLER, R. K., HEDGEPEETH, J. M., 'An Algorithm for Finite Element Analysis of Partially Wrinkled Membranes', *AIAA Technical Note 82-4293*, 1982
5. ADLER, A. L., MIKULAS, M. M., HEDGEPEETH, J. M., 'Static and Dynamic Analysis of Partially Wrinkled Membrane Structures', *AIAA-2000-1810*, 2000
6. KANG, S., IM, S., 'Finite Element Analysis of Wrinkling Membranes', *Journal of Applied Mechanics*, Vol. 64, 1997
7. LU, K., ACCORSI, M., LEONARD, J., 'Finite Element Analysis of Membrane Wrinkling', *International Journal for Numerical Methods in Engineering*, 50, 2001
8. BARNES, M. R., 'Form Finding and Analysis of Tension Structures by Dynamic Relaxation', *International Journal of Space Structures Vol. 14 No. 2*, 1999
9. HEPPEL, P., 'Accuracy in Sail Simulation: Wrinkling and growing fast sails', *Proceedings High Performance Yacht Design Conference*, 2002
10. GRAF, K., MÜLLER, O., 'Photogrammetric Investigation of the Flying Shape of Spinnakers in a Twisted Flow Wind Tunnel', *Proceedings 19th Chesapeake Sailing Yacht Symposium*, 2009
11. VIOLA, I. M., FLAY, R. G. J., 'Pressure Distributions on Modern Asymmetric Spinnakers', *Trans RINA, Vol. 151, Part B1*, 2009
12. PATON, J., MORVAN, H.P., HEPPEL, P., 'Fluid Structure Interaction of Yacht Sails', *Proceedings International Conference on Innovation in High Performance Sailing Yachts*, 2008
13. ANSYS, Inc, 'User Fortran', *ANSYS CFX-Solver Modelling Guide, Release 12.1, Chapter 16*, 2009
14. Press, W. H., Teukolsky, S. A., Vetterling, W. T., Flannery, B. P., 'Numerical Recipes in Fortran 90, THE Art of PARALLEL Scientific Computing', Second Edition, *Cambridge University Press*, 1996.